Why bumpy is better: The role of the dissipation distribution in slip flow over a bubble mattress

A. Sander Haase, Jeffery A. Wood, and Rob G. H. Lammertink[*]
*Soft Matter, Fluidics and Interfaces, MESA$^+$ Institute for Nanotechnology, University of Twente,
P.O. Box 217, 7500 AE Enschede, The Netherlands*

Jacco H. Snoeijer
*Physics of Fluids, MESA$^+$ Institute for Nanotechnology, University of Twente,
P.O. Box 217, 7500 AE Enschede, The Netherlands
and Department of Applied Physics, Eindhoven University of Technology,
P.O. Box 513, 5600 MB Eindhoven, The Netherlands*

It has been observed that the amount of effective slip for transverse flow over a bubble mattress is maximum for bubbles that protrude somewhat in the channel flow. In this paper we provide an explanation for this characteristic feature by analyzing the spatial distribution of viscous dissipation for bubbles of varying protrusion angles. Bubbles protruding in the channel act as obstacles and reduce the effective channel height, thereby increasing the viscous dissipation in the bulk flow. At small scales, however, our numerical analysis reveals that increasing the bubble protrusion angle reduces the dissipation near the contact points of the no-slip channel wall and the no-shear bubble surface. We obtain an analytical expression to quantify this effect based on classical corner flow solutions. The two antagonistic effects, decreased dissipation near the bubble corners and increased dissipation on larger scale, explain why the effective slip length is maximum for a bubble mattress that is slightly bumpy.

I. INTRODUCTION

Superhydrophobic surfaces are commonly used to optimize transport in microfluidic and nanofluidic systems [1–3]. The gas present in the microstructures of the slippery and water-repellent surfaces reduces the overall friction between a flowing liquid and the wall, compared to flat nonslippery surfaces. The menisci of the gas bubbles are often assumed to be shear-free. This leads to small but finite effective slip velocities at the interface, which can enhance interfacial transport. The amount of wall slip is commonly expressed by the slip length b, as expressed by Navier's law [4]. At the surface, $\mathbf{u} - b\partial_n\mathbf{u} = \mathbf{0}$. Here $\mathbf{u}$ is the liquid velocity and ∂_n is the derivative normal to the surface. When considering slip over superhydrophobic surfaces, b denotes the effective slip length experienced by the flow on scales larger than the bubbles.

For flat hybrid gas-solid surfaces, the effective slip length is always positive. This may not be true for superhydrophobic surfaces containing curved gas-liquid interfaces. For transverse flow over a bubble mattress as shown in Fig. 1, which is a two-dimensional superhydrophobic surface consisting of an array of no-shear gas bubbles with no-slip walls in between, the amount of slip strongly depends on the curvature of the bubble interface (defined by the protrusion angle ϑ, shown
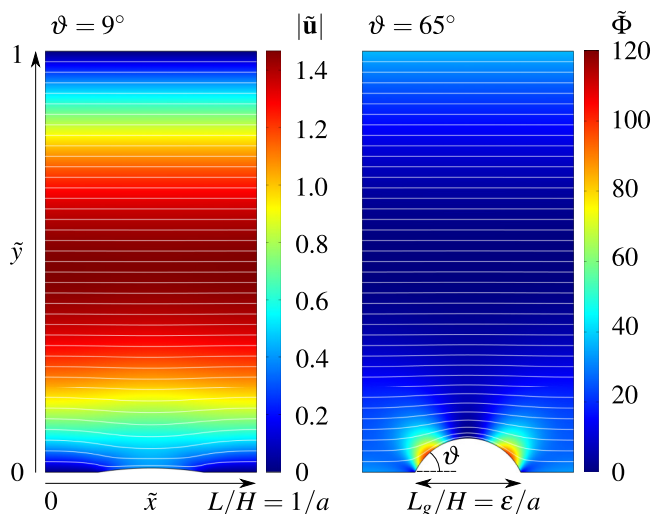
---

[*]r.g.h.lammertink@utwente.nl

FIG. 1. Geometry of a viscous flow over a bubble mattress. A no-shear bubble with a protrusion angle ϑ is sticking out into the channel flow at the lower boundary. The boundary conditions in the horizontal direction are periodic. In the left figure, the color map represents the velocity magnitude $|\tilde{\mathbf{u}}|$, while in the right figure the color map shows the local viscous dissipation rate $\tilde{\Phi}$. The white lines are streamlines of the velocity field $\tilde{\mathbf{u}}$. The relevant dimensions are the channel height H, the width of periodicity L, and the bubble size L_g. Throughout the paper, all length scales are nondimensionalized by the channel height H.

in Fig. 1). This dependence shows two characteristic features: Slip is maximum for a small but finite nonzero protrusion angle ϑ, but when the angle exceeds a critical value, the slip length becomes negative.

The first to demonstrate the existence of a critical protrusion angle for negative slip were Steinberger *et al.* [5]. They found that the slip length decreases when the protrusion angle ϑ increases. For strongly protruding bubbles, negative slip lengths were computed, implying that the flow is retarded by the superhydrophobic surface. Similarly, Legendre and Colin [6] showed that, compared to a nonslippery surface, wall drag always increases for linear shear flow over stationary, shear-free hemispherical bubbles.

The strong dependence of the effective slip length on the bubble protrusion angle ϑ was confirmed numerically by Hyväluoma and Harting [7]. They also found, considering infinitely long cylindrical bubbles, that the slip length strongly depends on the flow direction. When the flow is parallel to the bubble slots, the slip length b is always positive [8–10]. The streamlines are straight and no roughness is encountered by the flow. In the case of transverse flow, however, the slip length is negative when the protrusion angle exceeds a critical value. The surface is rough due to the protruding bubbles, giving rise to negative slip lengths.

Davis and Lauga [11] derived an analytical expression for the effective slip length for transverse shear flow over a bubble mattress in the dilute limit, i.e., for a surface porosity $\varepsilon \ll 1$. Their two-dimensional model showed good qualitative agreement with previous numerical results [5,7]. However, the theory by Davis and Lauga revealed a curious feature: The slip length is maximum for a small but nonzero optimum protrusion angle of $\vartheta = 14°$. For larger protrusion angles, the slip length decreases and becomes negative when ϑ exceeds the critical angle of $\vartheta = 65°$. Later studies confirmed the general validity of the model, even for a three-dimensional surface containing spherical bubbles [12–15].

Teo and Khoo [15] showed that the optimum and critical protrusion angles depend on the channel confinement, which is the ratio of channel height to projected bubble diameter. When increasing the confinement, the values of the optimal and critical protrusion angle decrease as the bubbles more

readily obstruct the flow in shallow channels. The confinement effect becomes stronger for high surface porosities. They also showed some characteristics of the flow field along the channel wall and the bubble surface to explain the phenomenon of negative slip. Their numerical results indicated that with increasing protrusion angle, the wall shear stress near the contacts points of wall and bubble decreases, while the static pressure difference between the front and rear halves of the bubble interface increases. This latter effect dominates beyond the critical protrusion angle, resulting in negative slip lengths. However, even though the existence of an optimal protrusion angle is very robust and consistently observed in theory and simulations, it remains an open question why for transverse flow over a bubble mattress the amount of slip is maximum for a finite nonzero protrusion angle.

In this paper we will provide an explanation why the effective slip length over a bubble mattress exhibits a maximum for a certain angle. To formulate an answer, we establish an explicit connection between effective slip and viscous dissipation and consider the spatial distribution of viscous dissipation. As the numerical and analytical results reveal, there are two opposing effects acting at different scales that result in an optimal angle for which the overall dissipation is minimum or the effective slip is maximum.

II. MATHEMATICAL FORMULATION

A. Governing equations

Figure 1 depicts the geometry of the system considered in this study. The periodic model with length L is two dimensional and the undeformable spherical bubbles are considered to be infinitely long. The top wall is nonslippery, while the bottom wall is a no-slip surface containing a no-shear bubble of width L_g and having a radius of curvature of $R = L_g/2 \sin \vartheta$. The protrusion angle ϑ of the bubble was varied. The ratio of channel height to domain length was set to $a = H/L = 2$. The porosity was fixed at $\varepsilon = L_g/L = 1/2$. Parametric studies on the relationship between geometry and effective slip have been published before [11,14,15]. Here we aim to identify the physical mechanism that leads to the existence of an optimal protrusion angle for which slip is maximum.

Assuming that the Reynolds number $\mathrm{Re} = u_{\mathrm{av}} \rho D / \mu$ is very small and that the flow is incompressible, momentum transport is described by the continuity and Stokes equations

$$\tilde{\nabla} \cdot \tilde{\mathbf{u}} = 0, \tag{1}$$

$$0 = -\tilde{\nabla} \tilde{p} + \tilde{\nabla}^2 \tilde{\mathbf{u}}. \tag{2}$$

Here $\tilde{\nabla} = (\partial_x, \partial_y)$, $\tilde{\mathbf{u}} = (\tilde{u}_x, \tilde{u}_y)$ is the velocity vector, and $\tilde{p}$ is the pressure. The equations were made dimensionless using the height-averaged velocity u_{av}, the channel height H, and the dynamic viscosity μ. The scaled variables thus read $\tilde{\mathbf{x}} = \mathbf{x}/H$, $\tilde{\mathbf{u}} = \mathbf{u}/u_{\mathrm{av}}$, and $\tilde{p} = pH/\mu u_{\mathrm{av}}$.

The no-slip boundary condition is applied to the solid walls at the top and the bottom,

$$\tilde{\mathbf{u}} = \mathbf{0}. \tag{3}$$

The bubble surface is nonpenetrable and shear-free, which is described by

$$\tilde{\mathbf{u}} \cdot \tilde{\mathbf{n}} = 0,$$
$$\{-\tilde{p}\mathbf{I} + [\nabla \tilde{\mathbf{u}} + (\nabla \tilde{\mathbf{u}})^{\mathrm{T}}]\} \cdot \tilde{\mathbf{n}} = \mathbf{0}. \tag{4}$$

The domain is periodic in the $\tilde{x}$ direction, i.e.,

$$\tilde{\mathbf{u}}(0, \tilde{y}) = \tilde{\mathbf{u}}(1/a, \tilde{y}),$$
$$\tilde{p}(0, \tilde{y}) = \tilde{p}(1/a, \tilde{y}). \tag{5}$$

The equations were solved numerically using COMSOL MULTIPHYSICS 5.0. The standard relative tolerance was 1×10^{-3}. Here $P2 + P1$ discretization (second-order elements for velocity and first-order elements for pressure) was used to solve the Stokes equations. The mesh was refined

near the walls by using a smaller mesh size and by using boundary layers, until the effective slip length became mesh independent. The complete mesh consists of approximately 15 500 domain elements and about 550 boundary elements. The numerical solution is obtained by imposing a pressure gradient. Owing to the linearity of the Stokes flow, the solution is subsequently scaled to achieve the desired average velocity of $\tilde{u}_{av} = 1$.

B. Relating the effective slip length to viscous dissipation

The reduction in flow resistance for a superhydrophobic wall is commonly quantified by an effective slip length. The effective slip length for a heterogeneously slippery surface is defined as the equivalent slip length required to achieve the same average velocity and pressure gradient past a homogeneous slip wall. Here we will briefly repeat the relevant definitions and establish a formal link between the slip length and the total viscous dissipation in the fluid domain. The latter will be used to explain the nonmonotonic dependence of the slip length on ϑ.

1. Effective slip length

For a plane channel with a one-sided homogeneous slip wall, the pressure-driven velocity field reads

$$\tilde{u}_x = \frac{1}{2}\frac{\partial \tilde{p}}{\partial \tilde{x}}\left[(\tilde{y}^2 - \tilde{y}) - \frac{\tilde{b}}{1+\tilde{b}}(1-\tilde{y})\right], \tag{6}$$

where $\tilde{b} = b/H$ is the scaled slip length. One verifies the no-slip condition $\tilde{u}_x = 0$ at the upper boundary $\tilde{y} = 1$, while at the lower boundary $\tilde{y} = 0$ the solution satisfies Navier's slip condition $\tilde{u}_x = \tilde{b}\partial_y\tilde{u}_x$. The corresponding average liquid velocity is

$$\tilde{u}_{av} = -\frac{1}{12}\frac{\partial \tilde{p}}{\partial \tilde{x}}\left(\frac{1+4\tilde{b}}{1+\tilde{b}}\right). \tag{7}$$

This can be rewritten as an explicit expression for the effective slip length $\tilde{b}$,

$$\tilde{b} = \left(-\tilde{u}_{av} - \frac{1}{12}\frac{\partial \tilde{p}}{\partial \tilde{x}}\right) \bigg/ \left(\tilde{u}_{av} + \frac{1}{3}\frac{\partial \tilde{p}}{\partial \tilde{x}}\right), \tag{8}$$

which was used to compute the slip lengths in our simulations of flow over a bubble mattress. For clarity we keep explicitly $\tilde{u}_{av}$ in the various formulas, even though our dimensionalization implies $\tilde{u}_{av} = 1$. Commonly in the literature, the slip length is nondimensionalized based on L_g, the width of the bubble. In the present notation this reads

$$\frac{2b}{L_g} = \frac{2a}{\varepsilon}\tilde{b}. \tag{9}$$

2. Viscous dissipation

To explain why slip is optimal for an angle larger than $0°$, it is useful to express slip in terms of the total viscous dissipation. The dimensionless viscous dissipation rate (per unit volume), in the case of incompressible flow, is given by [16,17]

$$\tilde{\Phi} = 2\left[\left(\frac{\partial \tilde{u}_x}{\partial \tilde{x}}\right)^2 + \left(\frac{\partial \tilde{u}_y}{\partial \tilde{y}}\right)^2\right] + \left(\frac{\partial \tilde{u}_y}{\partial \tilde{x}} + \frac{\partial \tilde{u}_x}{\partial \tilde{y}}\right)^2, \tag{10}$$

where $\tilde{\Phi} = \Phi H^2/\mu u_{av}^2$. The total dissipation in the two-dimensional domain is obtained by integrating $\tilde{\Phi}$ over the domain area A,
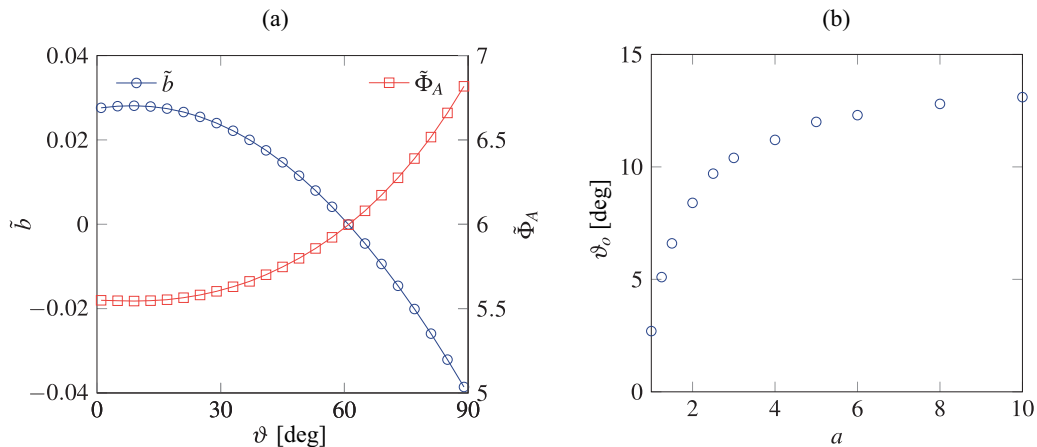
$$\tilde{\Phi}_A = \iint_A \tilde{\Phi}\, dA, \tag{11}$$

FIG. 2. (a) Dimensionless slip length $\tilde{b}$ and total dissipation $\tilde{\Phi}_A$ plotted as a function of the bubble protrusion angle ϑ for $a = 2$ and $\varepsilon = 1/2$. The effective slip length and the total dissipation are related to each other by Eq. (13). When $\vartheta = 9°$, $\tilde{b}$ is maximum and $\tilde{\Phi}_A$ is minimum. (b) Dependence of the optimal protrusion angle ϑ_o on the confinement factor $a = H/L$ for $\varepsilon = 1/2$.

where we use the convention that the subscript A implies an area integral of $\tilde{\Phi}$. Similarly, the dissipation in a streamtube $\tilde{\Phi}_{A,\mathrm{str}}$ is obtained by integrating $\tilde{\Phi}$ over the area between two streamlines A_{str}. Using Gauss's theorem [16], one can derive that

$$\iint_A \tilde{\Phi} \, dA = -\tilde{u}_x \Delta \tilde{p} \int_0^1 d\tilde{y} = -\frac{\tilde{u}_{\mathrm{av}}}{a} \frac{\partial \tilde{p}}{\partial \tilde{x}}. \tag{12}$$

By combination of Eqs. (11) and (12) and subsequent elimination of the pressure gradient using Eq. (7), the total dissipation in the domain can be expressed as

$$\tilde{\Phi}_A = \frac{12\tilde{u}_{\mathrm{av}}^2}{a} \left(\frac{1 + \tilde{b}}{1 + 4\tilde{b}} \right). \tag{13}$$

Importantly, this equation gives a direct monotonic relation between the effective slip length $\tilde{b}$ and the total viscous dissipation $\tilde{\Phi}_A$. As expected, a smaller dissipation implies a larger effective slip. Explaining why there exists a maximum in wall slip for a nonzero protrusion angle ϑ is therefore equivalent to understanding why there is a minimum in viscous dissipation at the same angle.

III. RESULTS AND DISCUSSION

We now show the results of our numerical simulations, based on which we propose an explanation for the existence of an optimal protrusion angle. Figure 2(a) displays the dimensionless slip length $\tilde{b}$ (blue circles), which is equivalent to $(\varepsilon/2a)(2b/L_g)$ according to Eq. (9), as a function of the protrusion angle ϑ. It reveals that slip is maximum for a finite positive protrusion angle of $\vartheta = 9°$ in this case. The same figure shows the corresponding total dissipation $\tilde{\Phi}_A$ (red squares) by the flow, which is related to the effective slip length according to Eq. (13). Maximum wall slip can indeed be expressed as minimum dissipation, since for the optimal protrusion angle ϑ_o of $9°$ the total dissipation is minimum.

The protrusion angle for which the effective slip length is maximum, or the overall dissipation is minimum, depends on the confinement of the channel and the coverage density of the surface by bubbles. Figure 2(b) illustrates that when the relative channel height is large, i.e., $a \gg 1$, the optimum protrusion angle converges to a value of $14°$ for $\varepsilon = 1/2$. This is similar to the optimum angle found by Davis and Lauga [11], although their expression is derived for shear flow over a
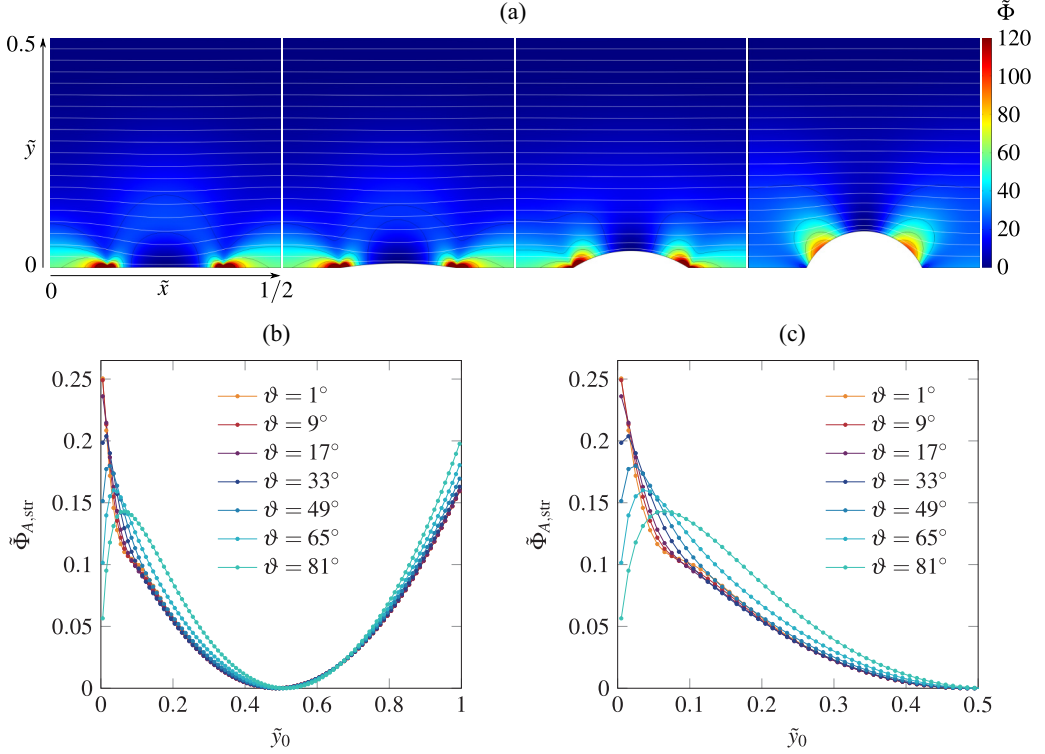
FIG. 3. The color map in (a) shows the distribution of the dissipation rate $\tilde{\Phi}$ for four different protrusion angles for $0 \leqslant \tilde{y} \leqslant 0.5$: from left to right, $\vartheta = 1°, 9°, 33°, 65°$. The streamlines of the velocity field $\tilde{\mathbf{u}}$ are shown in white. The black lines are contour lines of the dissipation rate $\tilde{\Phi}$. In (b) and (c) the viscous dissipation $\tilde{\Phi}_{A,\text{str}}$ in a streamtube of width $\Delta \tilde{y} = 0.01$ is plotted against the midpoint of the streamtube $\tilde{y}_0$ at $\tilde{x} = 0$. In (b) $a = 2$ and $\varepsilon = 1/2$ and (c) is a magnification of (b).

bubble mattress in the dilute limit ($\varepsilon \ll 1$). The existence of an optimum protrusion angle is therefore very robust, although the precise value depends on the geometry of the system.

To explain why the slip length is maximum for slightly protruding bubbles, we now consider the distribution of the viscous dissipation rate $\tilde{\Phi}$ in the fluid domain. These distributions are shown in Fig. 3(a) for several protrusion angles. The figures clearly show a gradual change of the spatial distribution of the viscous dissipation rate when increasing ϑ. For small angles the dissipation rate is strongest near the bubble corners, where the boundary condition changes discontinuously from no slip at the solid wall to no shear at the bubble surface. The fluid flow close to the surface is significant for small angles, giving rise to large velocity gradients and hence high dissipation rates near the discontinuities. When the protrusion angle increases, we observe that the location of maximum $\tilde{\Phi}$ gradually shifts upward along the bubble surface. Similar trends were observed by Theo and Khoo [15], who considered the shear stress and static pressure at the lower wall.

In order to compare the dissipation distribution for different protrusion angles more quantitatively, we consider the dissipation in a streamtube $\tilde{\Phi}_{A,\text{str}}$ versus the midpoint $\tilde{y}_0$ of the streamtube at $\tilde{x} = 0$. This is shown in Fig. 3(b), with a more detailed zoom given in Fig. 3(c). The dissipation profiles depend nonmonotonically on the height $\tilde{y}$, with a suppressed dissipation in the first few streamtubes ($\tilde{y}_0 < 0.05$), which are passing close to the corners of the bubble. The dissipation near the corner decreases considerably with increasing protrusion angle. This indicates that the fluid between the bubbles becomes nearly stagnant, supporting the notion by Steinberger *et al.* [5] of an immobilized liquid layer close to the wall for large protrusion angles.

On the other hand, farther away from the solid wall ($\tilde{y}_0 > 0.05$) the dissipation increases with ϑ. The location of maximum dissipation shifts from the contact points towards the front and rear edge of the bubble surface. First, the pressure difference over the bubble surface becomes larger when the protrusion angle increases [15]. Second, bubbles protruding in the channel increasingly form obstacles to the flow, acting as roughness elements [7]. These elements causing bending of the streamlines, which necessarily means that viscous dissipation increases. We also observe that for $\vartheta > 33°$ the dissipation increases near the upper wall. The strongly protruding bubbles reduce the effective channel height, leading to increased shear and higher dissipation rates in the bulk channel flow.

Figure 3 is key to understanding why there exists an optimum protrusion angle for which effective slip is maximum or viscous dissipation is minimum. Since $\tilde{\Phi}_A = \int \tilde{\Phi}_{A,\text{str}} \, d\tilde{y}$, this figure reveals that there are two opposing trends. Near the surface, in the corners between bubble and wall, the dissipation decreases with increasing ϑ, while globally the dissipation becomes larger with ϑ. These two competing effects lead to a minimum in total dissipation, and therefore maximum slip, at an optimum protrusion angle of, in this case, $\vartheta_o = 9°$.

We now explain in detail why viscous dissipation is suppressed near the bubble corner when the protrusion angle increases. This analysis is based on the analytical corner flow solutions by Moffatt [18], who solved the flow field of a viscous fluid near a sharp corner between a rigid boundary and a free surface. It turns out that viscous corner flows exhibit a universal self-similar structure that depends only on the boundary conditions (which are no slip and no shear in the present case) and on the corner angle. This allows us to compute the dissipation in the vicinity of the corner as a function of the protrusion angle ϑ. In terms of the stream function ψ, the Moffatt corner flow solutions in polar coordinates $(\tilde{r},\phi)$ are of the form [18]

$$\psi(\tilde{r},\phi) = Af(\phi)\tilde{r}^\lambda. \tag{14}$$

For given angle ϑ, the function $f(\phi)$ has a prescribed functional form (see Appendix A). Likewise, the exponent λ, which does not depend on ϕ, can be determined from an eigenvalue problem that amounts to solving

$$\sin 2\alpha(\lambda - 1) = (\lambda - 1) \sin 2\alpha, \tag{15}$$

where $\alpha = \pi - \vartheta$. The values of λ (solid line) are plotted as a function of ϑ in Fig. 4(a), showing that λ increases monotonically with the protrusion angle ϑ. The amplitude A in Eq. (14) cannot be determined from a local analysis of the corner flow, but depends on how the flow is driven far away from the corner.

We can now use the Moffatt solution to compute the dissipation rate near the corner. From Eq. (14), one can derive that

$$\tilde{\Phi} = A^2 g(\phi)\tilde{r}^{2\lambda-4}, \tag{16}$$

which gives the distribution of the dissipation rate. Appendix A can be referred to for the full derivation. The resulting dissipation field is again self-similar. An example of the dissipation field is given in Fig. 4(d) for the case where $\vartheta = 12°$. While $g(\phi)$ and λ are readily calculated and we therefore precisely know how they change with the protrusion angle ϑ, this is not the case for A: The amplitude of the corner flow depends on the large-scale characteristics of the flow, which requires a fully resolved flow field. For this purpose we numerically determined the amplitude A from the explicit form of the stream function by Davis and Lauga [11] for shear flow over a bubble mattress in the dilute limit (which is given in Appendix B for completeness). Obviously, the solution by Davis and Lauga should implicitly contain the universal flow structure expressed by Eq. (14) at small distances from the corner. This has been verified by fitting the Moffatt solution to the solution of Davis and Lauga, giving us $\lambda(\vartheta)$. The resulting values (circles) are superimposed on the analytical values (solid line) in Fig. 4(a). Subsequently, the product $Af(\phi)$ is plotted in Fig. 4(b) for various protrusion angles. Most importantly, it reveals that changes in the function $f(\phi)$ with ϑ are only minor and that the amplitude A is approximately constant for the range of ϑ considered.
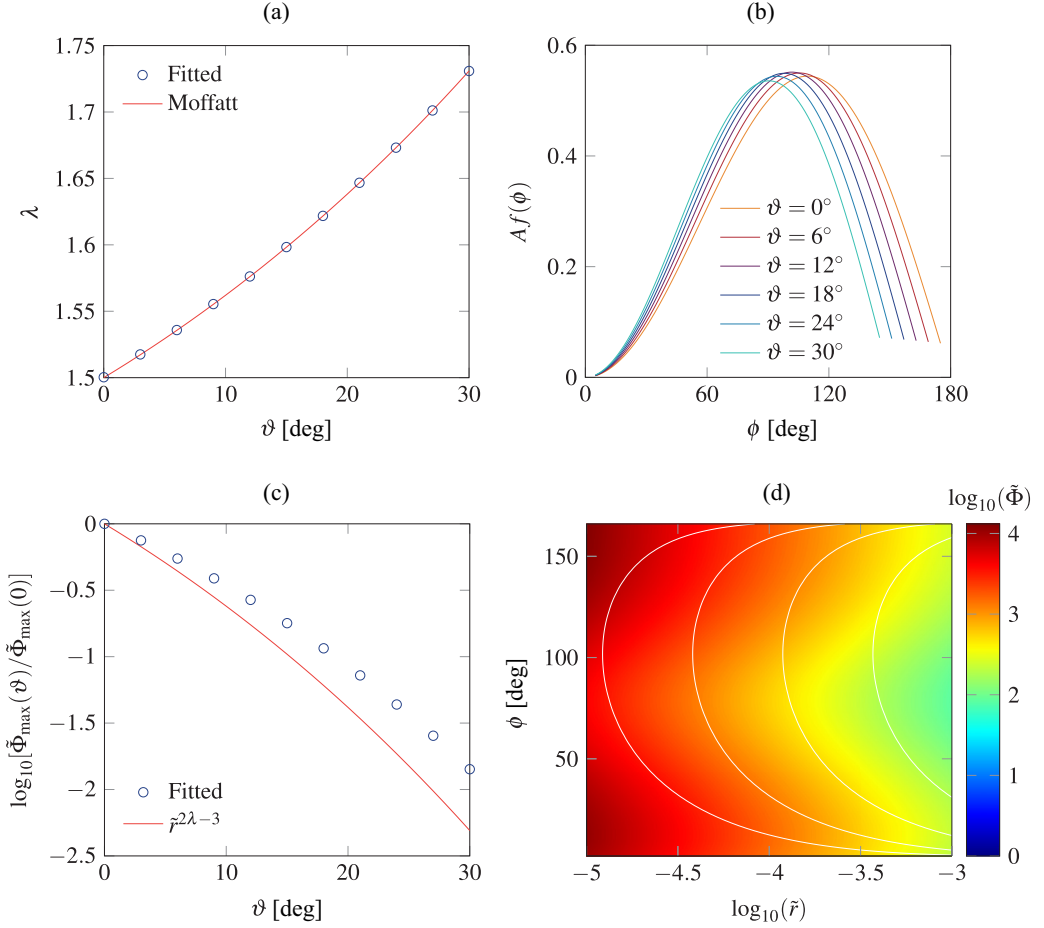
FIG. 4. To prove that the viscous dissipation in the vicinity of the bubble corners decreases with increasing protrusion angle ϑ, the flow near the corner is analyzed using the Moffatt corner flow solution $\psi = Af(\phi)r^\lambda$ [18]. (a) Exponent λ plotted as a function of ϑ, obtained from fitting the Moffatt solution to the analytical solution of Davis and Lauga [11] (circles) and by solving Eq. (15) (solid line). (b) Plot of $Af(\phi)$ for various ϑ. Both the amplitude A and the function $f(\phi)$ are approximately constant. (c) Maximum dissipation rate $\tilde{\Phi}_{max}(\vartheta)$, determined at $\tilde{r} = 10^{-5}$ and normalized by $\tilde{\Phi}_{max}(0)$. Based on a theoretical analysis, it is predicted that near the corner $\tilde{\Phi}(\vartheta)/\tilde{\Phi}(0) \sim \tilde{r}^{2\lambda-3}$ [Eq. (17)]. (d) Dissipation rate $\tilde{\Phi}$ for a protrusion angle of $\vartheta = 12°$, with some streamlines of $\tilde{\mathbf{u}}$ plotted in white. The bubble surface is located at $(\tilde{r}, 168°)$.

From the above considerations we infer that the dominant dependence of the dissipation rate $\tilde{\Phi}$ on the protrusion angle is encoded in $\lambda(\vartheta)$ and in particular in the dependence $\tilde{\Phi} \propto \tilde{r}^{2\lambda-4}$. To compare the viscous dissipation rate $\tilde{\Phi}$ at different protrusion angles ϑ, it is convenient to normalize $\tilde{\Phi}$ by the value of $\tilde{\Phi}$ for $\vartheta = 0°$. Since $\lambda = 3/2$ when $\vartheta = 0°$, we obtain

$$\tilde{\Phi}(\vartheta)/\tilde{\Phi}(0) \sim \tilde{r}^{2\lambda-3}, \tag{17}$$

which provides an analytical estimate of how the rate of dissipation depends on ϑ. The result is plotted as a solid line in Fig. 4(c) for $\tilde{r} = 10^{-5}$. The selected value of $\tilde{r}$ is arbitrary: As long as $\tilde{r} \ll 1$ the flow field is self-similar and graphs of Eq. (17) will exhibit the same trend. Figure 4(c) confirms that, as expected, in the direct vicinity of the corner the dissipation rate $\tilde{\Phi}$ strongly decreases with increasing protrusion angle. The numerically determined normalized dissipation rates (circles), obtained from the computed flow and dissipation fields utilizing the Moffatt solution
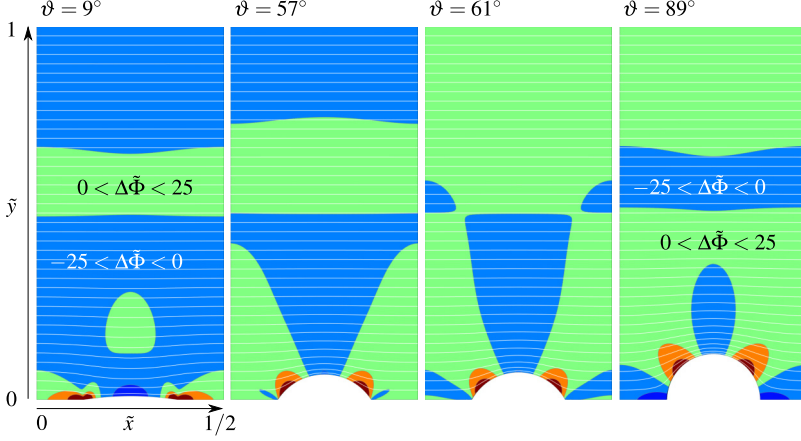
FIG. 5. For four different protrusion angles ϑ, the difference in dissipation rate $\Delta\tilde{\Phi} = \tilde{\Phi} - \tilde{\Phi}_{\mathrm{HP}}$ is plotted. Each contour level corresponds to $\Delta\tilde{\Phi} = 25$. Here $\Delta\tilde{\Phi} < 0$ for the blue contour levels and $\Delta\tilde{\Phi} > 0$ for the green and red contour levels. When ϑ is larger than the critical protrusion angle of, in this case, $61°$, in the channel mainly $\Delta\tilde{\Phi} > 0$, indicating increased friction with respect to Hagen-Poseuille flow through a nonslippery channel.

using the previously determined values of $A(\vartheta)$, are also plotted in Fig. 4(c). It shows that indeed the numerical values are well approximated by Eq. (17). The small differences between the calculated values and the analytical estimation can be attributed to the minor changes in the product $A^2 g(\phi)$ [and in particular to $g(\phi)$, since A is nearly constant] with protrusion angle ϑ. The corner analysis therefore explains that the suppressed dissipation near the bubble corners with increasing protrusion angle is mainly due to the increase of the exponent λ with the protrusion angle.

Finally, the dissipation distribution is not only valuable in explaining the existence of an optimal protrusion angle, it can also be used to predict the critical protrusion angle ϑ_c for which the slip length becomes negative. A negative slip length indicates that the friction for flow over a slippery surface is larger than for Hagen-Poiseuille flow through a smooth nonslippery channel. For Hagen-Poiseuille flow we find that $\tilde{\Phi}_{\mathrm{HP}} = 36(4\tilde{y}^2 - 4\tilde{y} + 1)$. This gives for a confinement factor of $a = 2$ an overall dissipation of $\tilde{\Phi}_A = 6$. This matches with Fig. 2, as $\tilde{b} = 0$ when $\tilde{\Phi}_A = 6$ for $\vartheta = 61°$.

To identify the critical protrusion angle, we consider the difference in local dissipation rate $\Delta\tilde{\Phi} = \tilde{\Phi} - \tilde{\Phi}_{\mathrm{HP}}$. Figure 5 shows $\Delta\tilde{\Phi}$ for four different protrusion angles. These plots again illustrate the fact that with increasing protrusion angle, the dissipation decreases near the corners of the bubbles and increases in the bulk channel flow. When increasing ϑ, for an increasing fraction of the channel $\Delta\tilde{\Phi}$ is positive (and therefore changes color from blue to green). Since for large protrusion angles the dissipation in the bulk flow is dominant over the dissipation near the bubble corners, the slip length should become negative when the dissipation in the main channel becomes larger than for Hagen-Poiseuille flow. Thus, when $\vartheta \geqslant \vartheta_c = 61°$ we expect that in the main channel $\Delta\tilde{\Phi} > 0$. Figure 5 confirms this expectation, as in the channel $\Delta\tilde{\Phi}$ is mainly negative (colored blue) when $\vartheta = 57° < 61°$ and predominantly positive (colored green) when $\vartheta \geqslant 61°$.

IV. CONCLUSION

The effective slip length for transverse flow over a bubble mattress is largest for bubbles that slightly protrude in the channel flow and not for completely flat bubbles. To explain the existence of this optimal protrusion angle, we established an explicit connection between the slip length and the viscous dissipation rate and subsequently analyzed the spatial dissipation distribution. The total dissipation in the domain can be directly related to the effective slip length.

The numerical results reveal that near the contact points of the no-slip wall and the no-shear bubble surface, the viscous dissipation rate is maximum when the bubbles are flat. The different boundary conditions of the wall and bubble give rise to large velocity gradients, leading to high dissipation rates. When increasing the bubble protrusion angle, the dissipation close to these discontinuities decreases. An analytical treatment of the dissipation rate in the corner utilizing a classical corner flow solution provides proof of this observation. On the other hand, bubbles sticking out into the channel flow act as obstacles and reduce the effective channel height, thereby increasing the dissipation in the bulk flow.

We conclude that increasing the protrusion angle of a bubble has two opposing effects: It reduces dissipation in the vicinity of the bubble corners, while it increases viscous dissipation in the bulk of the channel. This explains the existence of an optimum protrusion angle larger than $0°$ for which the total dissipation in the channel is minimum or the amount of effective slip is maximum.

APPENDIX A: DISSIPATION RATE FUNCTION

The Moffatt solution [18] for flow of a viscous fluid near a sharp corner is written as

$$\psi = Af(\phi)\tilde{r}^{\lambda}, \tag{A1}$$

with A being a certain prefactor and $f(\phi)$ being a function of the form

$$f(\phi) = P\cos\lambda\phi + Q\sin\lambda\phi + R\cos(\lambda-2)\phi + S\sin(\lambda-2)\phi, \tag{A2}$$

where P, Q, R, and S are arbitrary constants, determined by the boundary conditions. Using this solution, we can derive a function for the dissipation rate near the corner. In polar coordinates, the dissipation rate $\tilde{\Phi}$ is given by

$$\tilde{\Phi} = 2\left[\left(\frac{\partial\tilde{u}_r}{\partial\tilde{r}}\right)^2 + \left(\frac{1}{\tilde{r}}\frac{\partial\tilde{u}_\phi}{\partial\phi} + \frac{\tilde{u}_r}{\tilde{r}}\right)^2\right] + \left[\tilde{r}\frac{\partial}{\partial\tilde{r}}\left(\frac{\tilde{u}_\phi}{\tilde{r}}\right) + \frac{1}{\tilde{r}}\frac{\partial\tilde{u}_r}{\partial\phi}\right]^2. \tag{A3}$$

Since $\psi = Af(\phi)\tilde{r}^{\lambda}$,

$$\tilde{u}_r = \frac{1}{\tilde{r}}\frac{\partial\psi}{\partial\phi} = Af'\tilde{r}^{\lambda-1},$$

$$\tilde{u}_\phi = -\frac{\partial\psi}{\partial\tilde{r}} = -Af\lambda\tilde{r}^{\lambda-1}. \tag{A4}$$

This ultimately results in the following expression for $\tilde{\Phi}$:

$$\tilde{\Phi} = A^2\{2f'^2(\lambda-1)^2 + 2f'^2(1-\lambda)^2 + [f'' - f\lambda(\lambda-2)]^2\}\tilde{r}^{2\lambda-4} = A^2g(\phi)\tilde{r}^{2\lambda-4}. \tag{A5}$$

APPENDIX B: STREAM FUNCTION FOR SHEAR FLOW OVER A BUBBLE MATTRESS

For shear flow over a bubble mattress in the dilute limit, i.e., $\varepsilon \ll 1$, Davis and Lauga [11] solved the velocity profile. The stream function $\psi(\xi,\eta)$ is derived in a bipolar coordinate system with

$$x = \frac{c\sinh\xi}{\cosh\xi + \cos\eta}, \quad y = \frac{c\sin\eta}{\cosh\xi + \cos\eta}. \tag{B1}$$

Here $c = L_g/2$. The stream function ψ, which far away from the surface equals $\psi = \frac{1}{2}\gamma y^2$, is written as

$$\psi = \gamma c^2 \left[\frac{1/2 \sin^2 \eta}{(\cosh \xi + \cos \eta)^2} - \frac{\int_0^\infty f(s,\eta) \cos s\xi \, ds}{\cosh \xi + \cos \eta} \right], \tag{B2}$$

$$f = -A(s) \sin \eta \frac{\sinh s(\pi - \eta)}{s} + B(s) \left[\cos \eta \frac{\sinh s(\pi - \eta)}{s} + \sin \eta \cosh s(\pi - \eta) \right], \tag{B3}$$

γ being the shear rate. Here

$$A(s) = \frac{s}{\sinh 2s(\pi - \vartheta) + s \sin 2\vartheta} \left[\cos 2\vartheta + \frac{s \sin 2\vartheta \cosh s\pi + \sinh s(\pi - 2\vartheta)}{\sinh s\pi} \right] \tag{B4}$$

and

$$B(s) = \frac{s \sin 2\vartheta}{\sinh 2s(\pi - \vartheta) + s \sin 2\vartheta}. \tag{B5}$$

Besides the integration variable s, both A and B only depend on the bubble protrusion angle ϑ. The effective slip length of the bubble mattress is expressed as

$$\frac{2b}{L_g}(\vartheta) = \varepsilon \pi \int_0^\infty A(s) ds. \tag{B6}$$

---

[1] C. Neto, D. R. Evans, E. Bonaccurso, H.-J. Butt, and V. S. J. Craig, Boundary slip in Newtonian liquids: A review of experimental studies, Rep. Prog. Phys. **68**, 2859 (2005).

[2] J. P. Rothstein, Slip on superhydrophobic surfaces, Annu. Rev. Fluid Mech. **42**, 89 (2010).

[3] T. Lee, E. Charrault, and C. Neto, Interfacial slip on rough, patterned and soft surfaces: A review of experiments and simulations, Adv. Colloid Interface Sci. **210**, 21 (2014).

[4] C. L. M. H. Navier, Mémoire sur les lois du mouvement des fluids, Mem. Acad. Sci. Int. Fr. **6**, 389 (1823).

[5] A. Steinberger, C. Cottin-Bizonne, P. Kleimann, and E. Charlaix, High friction on a bubble mattress, Nat. Mater. **6**, 665 (2007).

[6] D. Legendre and C. Colin, Enhancement of wall friction by fixed cap bubbles, Phys. Fluids **20**, 051704 (2008).

[7] J. Hyväluoma and J. Harting, Slip Flow Over Structured Surfaces with Entrapped Microbubbles, Phys. Rev. Lett. **100**, 246001 (2008).

[8] D. Crowdy, Slip length for longitudinal shear flow over a dilute periodic mattress of protruding bubbles, Phys. Fluids **22**, 121703 (2010).

[9] C. J. Teo and B. C. Khoo, Flow past superhydrophobic surfaces containing longitudinal grooves: Effects of interface curvature, Microfluid. Nanofluid. **9**, 499 (2010).

[10] C.-O. Ng and C. Y. Wang, Effective slip for Stokes flow over a surface patterned with two- or three-dimensional protrusions, Fluid Dyn. Res. **43**, 065504 (2011).

[11] A. M. J. Davis and E. Lauga, Geometric transition in friction for flow over a bubble mattress, Phys. Fluids **21**, 011701 (2009).

[12] J. Hyväluoma, C. Kunert, and J. Harting, Simulations of slip flow on nanobubble-laden surfaces, J. Phys.: Condens. Matter **23**, 184106 (2011).

[13] E. Karatay, A. S. Haase, C. W. Visser, C. Sun, D. Lohse, P. A. Tsai, and R. G. H. Lammertink, Control of slippage with tunable bubble mattresses., Proc. Natl. Acad. Sci. USA **110**, 8422 (2013).

[14] A. S. Haase, E. Karatay, P. A. Tsai, and R. G. H. Lammertink, Momentum and mass transport over a bubble mattress: The influence of interface geometry, Soft Matter **9**, 8949 (2013).

[15] C. J. Teo and B. C. Khoo, Effects of interface curvature on Poiseuille flow through microchannels and microtubes containing superhydrophobic surfaces with transverse grooves and ribs, Microfluid. Nanofluid. **17**, 891 (2014).

[16] H. H. Winter, in *Viscous Dissipation Term in Energy Equations*, edited by J. R. Gordon, AIChE Modular Instruction Series C (American Institute of Chemical Engineers, New York, 1987), Vol. 7, Chap. C7.4, pp. 27–34.

[17] R. B. Bird, W. E. Stewart, and E. N. Lightfoot, *Transport Phenomena*, 2nd ed. (Wiley, New York, 2007).

[18] H. K. Moffatt, Viscous and resistive eddies near a sharp corner, J. Fluid Mech. **18**, 1 (1964).